Granular Matter (2018) 20:38
https://doi.org/10.1007/s10035-018-0809-y

ORIGINAL PAPER

Selection of material for X-ray tomography analysis and DEM simulations: comparison between granular materials of biological and non-biological origins

L. Babout[1] · K. Grudzień[1] · J. Wiącek[2] · M. Niedostatkiewicz[3] · B. Karpiński[4] · M. Szkodo[4]

Received: 8 December 2017 / Published online: 14 June 2018

Abstract
Physical properties and X-ray tomography images of five different granular materials: glass bead, glass grit, short grain white rice, sorghum and clay granules (Seramis) are investigated to select the most promising materials for numerical simulations and time-lapse X-ray tomography imaging. The examined materials represent granular materials of non-biological origin (glass bead, glass grit and Seramis) and granular plant materials (rice and sorghum). The choice of materials was dictated by their mechanical and packing properties, on one hand, and 3D imaging qualities of granular materials and quantitative particle shape analysis, on the other hand. It was found that materials of biological origin, i.e. rice and sorghum, showed promising characteristics and may be considered as the most appropriate materials for comparison between time-lapse X-ray tomography experiments and numerical simulation.

Keywords Granular materials · Physical properties · Geometrical properties · X-ray tomography

List of symbols

ρ_s	Density (kg/m^3)
$\mu_{s,w}$	Particle-wall friction coefficient (–)
E_s	Young modulus of single grain (MPa)
$\rho_{b,p}$	Poured density (kg/m^3)
$\rho_{b,t}$	Tapped density (kg/m^3)
$\rho_{b,csX}$	Bulk density at consolidated stress X (kg/m^3)
s_b	Compressibility ratio (%)
Φ_b	Natural angle of repose (°)
η	Porosity (–)
$\Phi_{b,i}$	Angle of internal friction (°)
$\Phi_{b,eff}$	Effective angle of internal friction (°)
c	Cohesion (kPa)
$\Phi_{b,w}$	Wall friction angle (°)
E_b	Young modulus of bulk material (kPa)
ν	Poisson's ratio (–)
C	Contrast coefficient (–)
μ	Linear attenuation coefficient (m^{-1})
F_{ab}, F_{ac}	Aspect ratios of 3D object (–)
V_p	Volume of object (voxels)
V_c	Volume of coffin box (voxels)
γ	Ellipsoidal shape goodness (–)

✉ L. Babout
Laurent.babout@p.lodz.pl

1 Institute of Applied Computer Science, Lodz University of Technology, Lodz, Poland

2 Institute of Agrophysics, Polish Academy of Sciences, Lublin, Poland

3 Faculty of Civil and Environmental Engineering, Gdańsk University of Technology, Gdańsk, Poland

4 Department of Materials Science and Engineering, Gdańsk University of Technology, Gdańsk, Poland

1 Introduction

Investigation of granular materials has been driving research and development interest for decades, so as to better understand mechanics an interparticle interactions during different technological processes. There are numerous types of processes involving granular materials (e.g. compression, shearing, sintering, silo filling and silo discharge), and bulk solids appear in various forms (e.g. dry grains and powders, slurries, suspensions or pastes), which make the spectrum of investigation of granular materials very large. A review of the literature reveals that various granular materials, used to different industrial processes, have been investigated over last few decades. The studies were conducted for grain beddings composed of particles of different geometrical and

mechanical properties. The studies included grain beddings composed of small particles with submillimeter size [1–5] and the ones comprising larger elements [6–10]. Properties of granular assemblies were found to be different due to their origination. Granular materials of biological origin (e.g. seeds and grains), commonly used in agriculture and food engineering, reveal mechanical characteristics different than the ones obtained for mineral or plastic granular materials. Granular plant materials are usually hydroscopic and change their mechanical properties through the absorption of moisture [9,11]. Their peculiar behavior requires both, specific approach in determining the parameters and specific setup of simulations. A review of the literature shows that numerous studies have been performed so far to measure material properties of particulate materials; however, values of parameters for materials of biological origin are uncertain and dispersed across various reports [11].

For many years, extensive efforts have been made to examine properties of granular packings and analyze effects occurring in grain bedding by using experimental methods; however, in many cases, these methods appeared to be insufficient. Because experimental methods do not provide essential insight into the properties of particulate assemblies and interactions between grains, non destructive imaging methods such as X-ray tomography and computational approaches are increasingly employed to examine granular media.

Granular materials, as porous materials, are genuinely good candidates for X-ray tomography studies because of strong contrast between matter and air. In that respect, it has opened new explorations of long-term researches related to particle packing, interaction, movement, strain localization or shear zone formation during compaction, uni-/multi-axial compression [12–17], shearing conditions [18–20] or gravitational flow [3,4,21].

In mechanics and physics, two different approaches can be used to describe and model granular materials [22]. The first approach is based on continuum theory and relies on empirical assumptions about the macroscopic material behavior. The second approach, in which the macroscopic analysis is complemented by a microscopic description of the material, enables modeling individual particles and their interactions. Application of computational techniques for modeling mechanical processes involving particulate solids requires knowledge of their structural and mechanical properties. That requirement frequently results in problems with selection of research material. A selection of material is not easy matter, since it can be governed by constraints, which are sometimes not compliant. For instance, application of numerical method such as discrete element method (DEM) is mainly constrained by number and shape of modelled particles. Bharadwaj [23] reported that current models were restricted to modelling 1 million spherical particles which could be considered to be a limit number of particles in DEM simulations. The degree of complexity increases when taking into account secondary forces (e.g. cohesion), non-spherical shapes of particles, mobile and flexible boundaries or complex contact force models. Among the many parameters which determine effectiveness of the discrete element method, material density and size of particle are important parameters also for an X-ray tomography experiments. It is commonly assumed that the scanned object of interest should be defined by at least 10 voxels along its minimum principal direction in order to be easily detected and processed. This is also directly correlated with the X-ray tomography spatial resolution in use. Last but not least, mechanical properties such as Young modulus or Poisson's ratio, static friction and internal friction angle are important parameters to consider for flow process control, which, combined with particle shape considerations, can lead to sliding or rolling motion during silo discharging [24,25].

The present project focuses on a multi-parameter approach to select materials that fulfill requirements regarding mechanical, physical and geometrical properties of grain beddings for X-ray tomography experiments and numerical simulations based on the Discrete Element Method. The study was performed for glass beads, glass grits, clay granules, and rice, and sorghum seeds, which represent granular materials of non-biological and biological origin, respectively. While glass beads, glass grits and clay granules are commonly used in the building industry, rice and sorghum are important materials for agriculture and food industry. A detailed analysis of properties of selected particulate materials can provide some hint for researchers to select research material for numerical simulations and X-ray tomography experiments.

The paper is organized as follows: the next section presents the different experimental set-ups used for investigation of material properties. Comparative results are analyzed and discussed in Sect. 3 before concluding remarks.

2 Experimental set-up

2.1 Research material

The present study has considered a comparison of five granular materials, which differ in origin, shape and chemical structure, but exhibit some similarities in size. Glass bead and grit, representing materials of non-biological origin, are made of the same silica glass type, i.e. soda-potassium glass with barium additive (SiO_2: 0.694–Na_2O: 0.104–K_2O: 0.063–BaO: 0.031–B_2O_3: 0.108). Monodispersed spherical glass marbles with average diameter of 3 mm has been chosen, while the glass grits had irregular shapes and size range similar to glass spheres. These materials are often considered for friction/shear studies [26–28], packing studies [29,30], gravitational flow experiments [31–33] and numerical mod-

eling [6,28,31,33,34]. Among the materials of non-biological origin, Seramis was also examined, which is composed of highly porous, processed clay granules. Seramis is composed of kaolinite ($Al_2Si_2O_5(OH)_4$), illite (K,H_3O) and quartz, which has very high water retention qualities.

The second type of research material included granular plant materials: rice and sorghum seeds. These granular media has also been considered in many research projects, since numerous studies of silo design and discharge are related to agricultural applications [8,35–39]. Short grain white rice and sorghum has been selected because of a size range corresponding to size of glass bead.

2.2 Physical property measurements

Different physical properties, such as density, Young Modulus, Poisson's ratio and coefficients of friction have been measured for single grain and bulk material, which determine behavior of granular materials. A method for determination of densities of glass beads, glass grit and seeds was based on the Archimedes' principle, which is one of the most commonly recommended methods for measuring densities of materials of irregular size and shape. A measurement of density of Seramis was conducted for samples placed in cylindrical chamber of volume of146 cm^3, by using a Helium pycnometer. Determination of density of Seramis was performed according to *ISO* recommendations. The elastic moduli and Poisson's ratios of single grains were measured with a material testing machine LLOYD Instruments, as recommended by *ASAE Standards* [40]. The densities of consolidated materials, and mechanical and frictional parameters of bulk materials were measured during uniaxial compression testing, according to *Eurocode* 1 recommendations [41]. Measurements were made for samples placed in cylindrical chamber of diameter of 6 cm and height of 2.55 cm. Additionally, frictional properties of selected materials were determined in direct shear test. A Jenike shear tester was used to measure particle-particle and particle-wall friction coefficients for the granular materials and Plexiglas sheet. Plexiglas material is frequently used for X-ray tomography in situ tests, because of its low X-ray attenuation coefficient, high mechanical strength to sustain load or normal pressure and abrasion resistance.

2.3 X-ray computed tomography

The task of X-ray computed tomography (XCT) is to reconstruct an object cross section that is related to a so-called attenuation map. The X-ray beam passing through the layer of matter is weakened by dissipation and absorption. It involves irradiating a sample with a small X-ray source and acquiring a series of radiographs while the object is rotated through 360° in equally spaced steps. A radiograph corresponds to a map of the transmitted intensities. This is detected by an imaging ADC device with a linear response, and is related to the integral attenuation of the different phases composing the object. For a specific energy and for a given pixel sensitivity of the detector, the intensity attenuation is given by the Beer–Lambert law as follows:

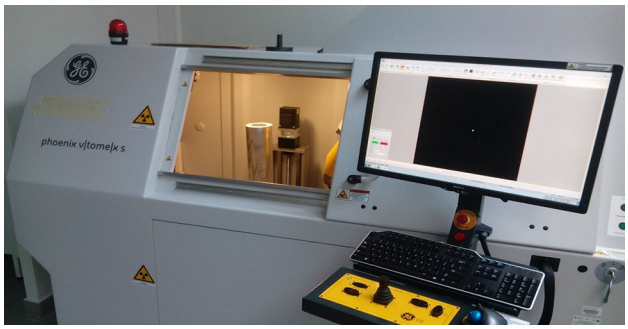

Fig. 1 General view of the GE phoenix v|tome|x s240 CT equipment used for scanning selected granular materials (color figure online)

$$I = I_0 \cdot exp\left(-\int_{X-ray\ path} \mu\,(l)\,dl\right), \tag{1}$$

where I is the beam intensity after passing through the medium; I_0 is the intensity of the incident beam; $\mu(l)$ stands for the attenuation coefficient of the examined material as a function of the X-ray path l, i.e. from the source to the considered pixel.

After the acquisition of the series of radiographs, a standard filtered back projection algorithm is usually used to reconstruct the 3D map of the attenuation coefficient [42,43]. The value of this coefficient is related to the nature and the density of the absorbing material, its atomic number as well as the selected X-ray energy [44]. As a result, for single phase material and a given energy, the linear attenuation coefficient is proportional to the local density of the material.

In this particular study, the granular material samples were scanned using the Phoenix v|tome|x s240 X-ray computed scanner, which is a versatile high-resolution system for 2D X-ray inspection, 3D failure and structure analyzes. A view of the equipment is shown in Fig. 1. Table 1 summarizes the different experimental conditions used to scan the five tested granular materials. The X-ray energy for glass materials was larger than the one applied for the other materials, because of larger density of glass. The X-ray energy level was also chosen for an X-ray transmission value of about 20% along the longest dimension of the cross-sectional area for all scanned granular materials.

The data were collected and processed using *Phoenix datos|x 2 acq* software, but for the reconstruction, *Phoenix datos|x 2 rec* has been used. The reconstruction strategy is based on the well-known filtered-back projection algo-

Table 1 Experimental setup for scanning different granular materials

	Voltage (kV)	Current (μA)	Filter	Exposure time (ms)	Voxel size (μm)
Glass bead	210	190	0.5 mm Cu	200	115
Glass grit					
Rice	170	130			
Sorghum					
Seramis					

rithm [43]. This reconstruction platform also includes a wide variety of modules for optimizing CT results for superior precision and quality, especially a beam hardening module. In the present case, a beam hardening correction factor of 7.2 was used for each tested materials. Reconstructed data were further processed and analyzed using *Matlab R2013a* and *Amira* 5.2. Note that the radiographs and reconstructed volumes of all tested materials presented in this paper are made available under ODC Attribution Licence [45].

3 Results and discussion

3.1 Electron microscope observations

Secondary Electron Microscopy (SEM) images of various granular materials at different magnifications are shown in Fig. 2 to reveal surface characteristics. While the surface of the glass bead is perfectly smooth (despite observations of small cavities), glass grit has a sharp edges and smooth surfaces in the length–width plane (Fig. 2b). Highly magnified images of rice and sorghum reveal a presence of an oily layer at their surface. White rice grain is characterized by compact structure, without any clear visible capillaries and dents. In the case of sorghum, longitudinal recesses centered radially at the pole of spheroid grains are visible (Fig. 2d). The width of the recesses is 10 μm with a maximum depth of 5 μm. Seramis has an irregular shape with structure similar to pumice (Fig. 2e). A high number of pore spaces with diameters ranging from 5 to 20 μm can be observed on the surface of this material.

3.2 Physical properties

The following analysis concerns physical properties of both, single grain and bulk material. Glass bead is taken as the reference material for the comparisons.

Results for single grains of the five tested granular materials are shown in Table 2. The results show that glass bead and glass grit have similar densities; however, density of the latter one is smaller by about 3%. Seramis grain has the highest density, which is about 20% higher than reference material. This is associated with its chemical composition, which contains potassium-based illite that is denser than the other silicate-based chemical components. Rice and sorghum have similar densities, which are about 50% smaller than the one measured for reference material. As far as particle-wall friction coefficient $\mu_{s,w}$ is concerned, among all tested materials, the smallest value of parameter was obtained for glass grit. In turn, the largest particle-wall friction coefficient was obtained for Seramis (i.e. above 30% larger than for glass), which was due to its rough and porous structure. It can be noticed that rice and sorghum have similar friction coefficients and elastic properties, which are, respectively, around 20 and 25% larger than the ones determined for reference material. The $\mu_{s,w}$ value for glass grit is smaller than one measured for glass marble and for natural materials, despite its highly irregular shape and sharp edges. This can be explained by its flake-like shape and opposite planes with smooth surface (see Fig. 2b), which slide down easier on Plexiglas plane during friction tests. An analysis of elastic properties of examined materials has shown that Seramis had the smallest Young modulus, which was due to its porous nature. It is worth highlighting that the Young modulus of glass grit was about 74% smaller than the one determined for the reference material, which can be attributed to its highly non-isotropic shape and heterogeneous structure of glass grit resulting from cracks (see Fig. 2b).

Figure 3 and Table 3 present physical/mechanical properties for the bulk materials. It can be observed in Fig. 3 that all bulk density profiles increase with increasing consolidation stress, but at different rates between 0 and 100 kPa of consolidation stress: it corresponds to about 0.55 for glass materials, around 0.3 for biological materials (white rice and sorghum) and about 0.1 for Seramis. In the case of glass grit, the bulk density is smaller w.r.t. glass bead by about 10%. White rice and sorghum have similar bulk density values, which is more than two times larger than the one measured for Seramis. The different values of compressibility ratio s_b, which is the relative difference between tapped and poured densities, were also obtained for various materials. In the case of bulk solids composed of irregularly shaped grains, such as glass grit and Seramis, s_b equals to 5% and is almost twofold higher than value of the compressibility of the glass bead. In turn, the organic materials (i.e. white rice and sorghum) are characterized by a much greater compressibility ratio, equaled to

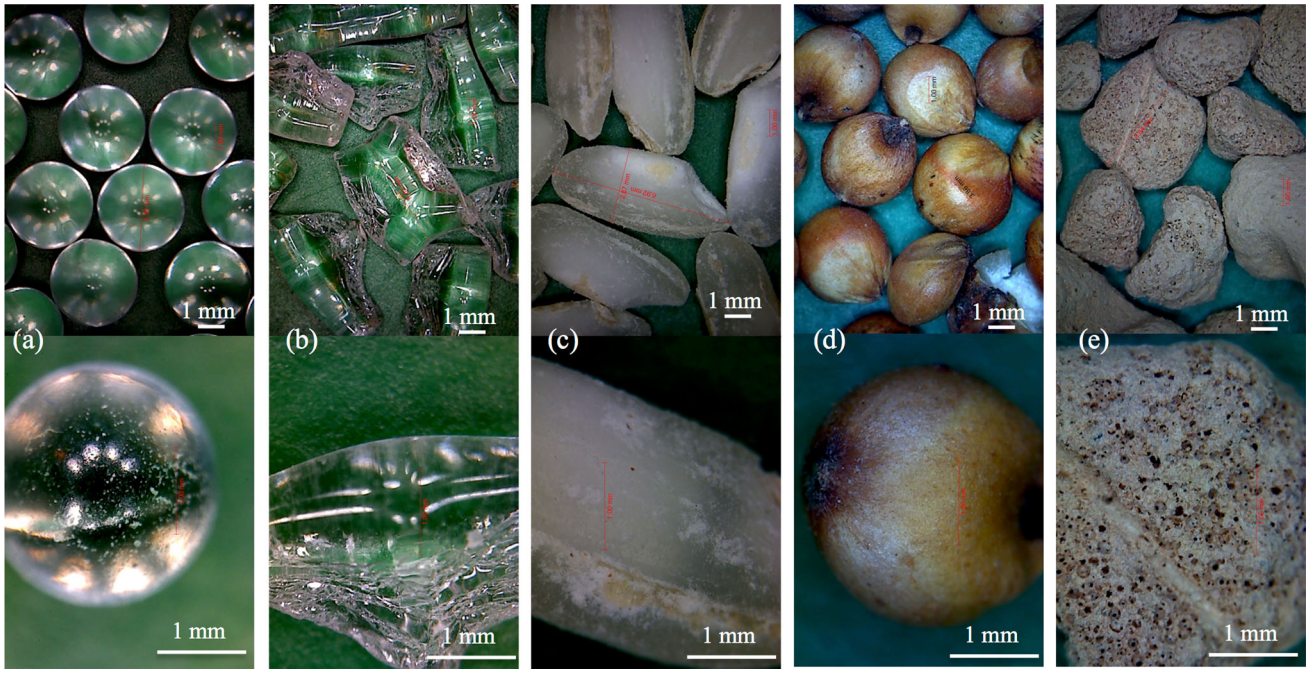

Fig. 2 SEM images of the tested granular materials at 2 magnifications (top: ×15, bottom: ×115). **a** Glass bead, **b** glass grit, **c** white rice, **d** sorghum and **e** Seramis (color figure online)

Table 2 Summary of results of laboratory tests for a single grain

	Glass bead	Glass grit	Rice	Sorghum	Seramis
ρ_s (kg/m^3)	2249	2180	1338	1084	2741.5*
	(± 1.25)	(± 15)	(± 18)	(± 74)	(± 7)
$\mu_{s,w}$ (°)	0.384	0.336	0.403	0.417	0,449
	(± 0.029)	(± 0.020)	(± 0.021)	(± 0.049)	(± 0.043)
E_s (MPa)	66,500	17,500	98.4	92.4	29.6
	(± 1330)	(± 1320)	(± 23.8)	(± 9.3)	(± 4.7)

Standard deviation values are shown in brackets ()
*Density measured with helium pycnometer

8.6%. A smaller porosity was obtained for isotropic or nearly isotropic materials like glass beads and sorghum, as compared to materials composed of irregularly shaped grains, such as glass grit or white rice. These results corroborate to findings of Cho et al. [46] who reported that irregularity hinders particle mobility and their ability to attain dense packing configuration. In this study, the porosity of granular packing comprising Seramis was not determined, due to difficulties resulting from porous nature of Seramis grains.

A comparison of frictional properties of examined materials has also provided interesting results, which confirmed an effect of cohesiveness and shape of particles on macroscopic friction coefficient in granular assemblies [47–49]. Glass grit, which has the largest natural angle of repose Φ_b, is characterized by an internal friction angle $\Phi_{b,i}$ only 10% larger than the one determined for reference material. This is probably linked with the morphology of the grits that have polished sides. Interestingly, the glass grit also exhibits an increase

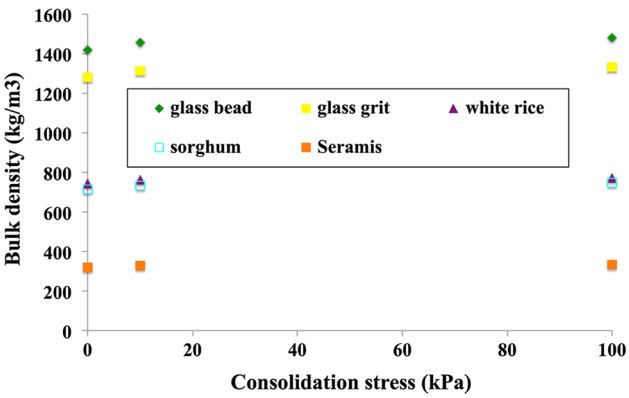

Fig. 3 Bulk density of the five tested materials for different consolidation stresses (color figure online)

of the wall friction angle $\Phi_{b,w}$ by about 14.75% w.r.t. glass bead, which is of similar magnitude as for $\mu_{s,w}$. It can be

Table 3 Summary of results of laboratory tests for bulk materials

	Glass bead	Glass grit	White rice	Sorghum	Seramis
$\rho_{b,t}$ (kg/m^3)	1555 (± 4.5)	1430 (± 14)	871 (± 4)	832 (± 7.5)	358 (± 3)
$\rho_{b,p}$ (kg/m^3)	1509 (± 2.5)	1358 (± 11)	797 (± 6.5)	760 (± 22)	325 (± 2.5)
s_b (%)	3.0 (± 0.5)	5.0 (± 0.7)	8.6 (± 0.35)	8.6 (± 1.8)	5.0 (± 3.2)
Φ_b (°)	13.9 (± 0.6)	44.7 (± 2.5)	33.0 (± 0.4)	30.4 (± 0.5)	39.0 (± 4.0)
η (–)	0.393 (± 0.001)	0.432 (± 0.019)	0.476 (± 0.006)	0.357 (± 0.027)	
$\Phi_{b,i}$ (°)	31 (± 0.3)	34.3 (± 2.9)	33.5 (± 1.8)	25.4 (± 1.9)	48.9 (± 9.2)
$\Phi_{b,eff}$ (°)	31.4 (± 5.6)	37.9 (± 6.4)	35.7 (± 6.1)	28.5 (± 5.2)	55.1 (± 9.1)
c (kPa)	0.095	0.92	0.58	0.67	2.63
$\Phi_{b,w}$ (°)	16.1 (± 0.9)	18.9 (± 0.4)	15.7 (± 0.2)	13.8 (± 0.6)	26.4 (± 0.6)
E_b (kPa)	4119 (± 247)	5676 (± 76.5)	4522 (± 447)	3246 (± 265)	4350 (± 73)
ν (–)	0.36 (± 0.01)	0.2 (± 0.02)	0.2 (± 0.01)	0.3 (± 0.02)	0.18 (± 0.02)

Standard deviation values are shown in brackets ()

also observed that sorghum has the second smallest angle of repose after glass bead and the smallest $\Phi_{b,i}$ and $\Phi_{b,w}$ values, which are, respectively, 18 and 14% lower than the one determined for glass bead. These small values of angle of repose and friction angles are due to oily film that has been observed in SEM images, combined with the spheroid shape of the grains. Despite its fragility, Seramis has the largest friction angles and the second largest angle of repose, which is due to its porous rough surface and irregular shape. It also has the largest cohesion value ($>$ 2.5 kPa), while glass bead, rice and sorghum can be considered as cohesionless materials. Regarding mechanical properties, differences between results obtained for single grain and bulk materials can be also observed. For instance, a Young modulus of Seramis grain is about 95% lower than the one determined for a single glass marble. However, at the level of the bulk material, this difference is reduced to about 12%. Interestingly, the Young modulus E_b of grain assembly composed of glass grit is larger by 12% than the one calculated for glass bead, despite being smaller by 75% at the level of grain. Regarding the natural materials, elastic modulus of grain bedding composed of white rice is similar to one determined for the reference material ($<$ 10%), while E_b value for sorghum is smaller by 34%. Simultaneously, single grains of these materials have similar elastic properties.

3.3 X-ray tomography analysis

3.3.1 Image contrast evaluation

The first part of the X-ray tomography analysis concerns the suitability of the selected granular materials for further quantitative studies related to concentration changes, individual particle and packing characterizations. Besides a particle size that is in agreement with the spatial resolution of the X-ray device, a good contrast between the granular material and the surrounding air is a required condition to facilitate material segmentation. Therefore, the first basic analysis concerns intensity histogram of the reconstructed raw volumes, before any image enhancement such as equalization or filtering are applied to increase image contrast. Figure 4a shows that all materials present two strongly separated peaks that correspond to air and granular materials. Seramis presents the case where the peaks are the closest, while glass grit corresponds to the opposite case. This is related to values of bulk density shown in Table 3, but also to the use of stronger X-ray energies for the two glass materials as compared to the other granular materials. Sorghum and rice have very similar histograms due to their similar chemical composition. However, in the case of glass materials, different histograms were obtained, since glass grit has its intensity peak shifted to the right, indicating a more pronounced X-ray absorption as compared to glass bead. This goes somehow against the fact that both materials have theoretically the same chemical composition and similar density, as presented in Table 2. Table 2 shows that density of glass grit is smaller by 3% than density of glass marble. It is expected that a further analysis, involving X-ray photoelectron spectroscopy, could bring some clarifications. However, this difference in X-ray absorption is of importance to quantitative analysis, as it is discussed hereafter in Sect. 3.4.

Usually, images are quantified after contrast has been enhanced. As mentioned previously, this can be simply done by applying histogram equalization, as it is illustrated in Fig. 4b. The contrast level in the image can be easily calculated from the histogram, using the following expression:

$$C = \frac{I_{max} - I_{min}}{I_{max} + I_{min}}, \tag{2}$$

where I_{min} and I_{max} are the modal values for the population of the lowest and the largest intensities, respectively, as

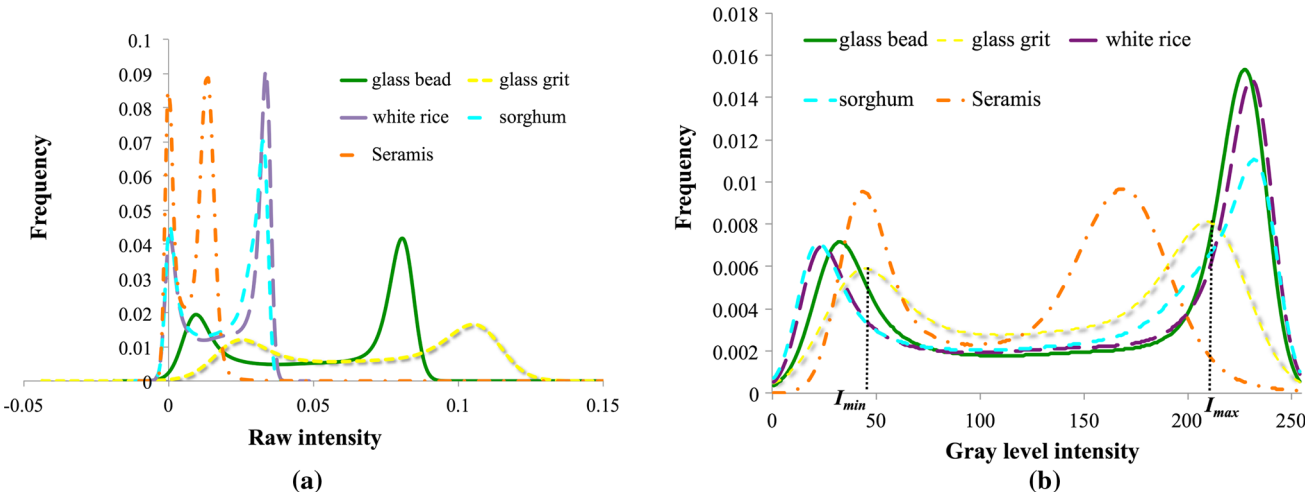

Fig. 4 Intensity histogram of the five tested materials **a** from raw data, **b** after 8-bit conversion and intensity equalization (color figure online)

illustrated in Fig. 4b for glass grit. The comparison of histograms obtained for five different granular materials shows that the largest contrast is found for white rice and sorghum ($C = 0.82$) while the lowest one is observed for Seramis ($C = 0.58$). Moreover, a larger contrast value is found for glass bead ($C = 0.76$) than for glass grit ($C = 0.65$).

Cross-sections of the different tested materials are shown in Fig. 5, after volume intensity ranges have been equalized and rescaled to 8-bit (i.e. intensity value between 0 and 255). One can notice the difference in shape of the granular materials, that is spheroid for glass bead and sorghum, ellipsoid for white rice and irregular shape for glass grit and Seramis.

A first qualitative analysis indicates that all materials have similar cross-sectional size range (i.e. $\sim$ 3 mm), except Seramis that has larger grains. Also, Fig. 5f shows an example of granular mixture of glass bead and glass grit (4% in mass) to illustrate the difference of contrast between the two materials discussed above (Fig. 4b). The images also show contours of grains in red after manual thresholding have been applied for segmentation. No particular advance segmentation method was needed due to the good contrast revealed by the intensity histograms. However, the particle packing induces strong contact between grains in the X-ray tomography images and their individual study needs a digital separation approach to be applied. The watershed algorithm has been applied numerous times for X-ray tomography images [29,50–54] of granular materials and proved to be an efficient method to separate convex monodispersed objects, but limited for more irregular particulate systems and usually associated to other post-processing method. For instance, the combination with level-set method [51] and contour probability map (stochastic watershed) [54] are good alternatives to refine shape and make extraction more reliable. However, both proposed method are time consuming and would show performance limitation for large volume data.

In the present case, authors have chosen classical marker-based watershed method [55], but with a pre-processing emphasis on selecting good island markers. For that, the following strategy has been chosen:

- local region minima, which are related to catchment basin revealed by inversed Euclidean distance map (see Fig. 6a) for each voxel of the segmented granular objects to the "air" background, are extracted and a histogram of their distance is computed, as shown in Fig. 6b.
- The largest bin distance corresponding to the frequency that is 75% of the histogram mode is used as a threshold distance value, as shown in Fig. 6b, below which corresponding voxels are considered as markers and set with the same inversed distance value, i.e. the one of the histogram mode.

This procedure creates large patches or island markers, as shown in Fig. 6c, which facilitate the region growing stage of the watershed approach. One can judge on Fig. 6d–e how the method improves the separation of the sorghum grains when compared with the original approach. Typical 3D rendering of the different granular materials are also shown in Fig. 7 to support the overall applicability of the method. Inspection of the data shows that around 10% of the grains are over-segmented, if one excludes particles that touch the region of interest (ROI) borders. Work is in progress to improve the algorithm by including feature classification in order to isolate over-segmented particles, which need further processing steps.

3.3.2 Particle shape analysis

After separation of all grains in the image processing step, a shape analysis can be made in next stage. The main purpose of

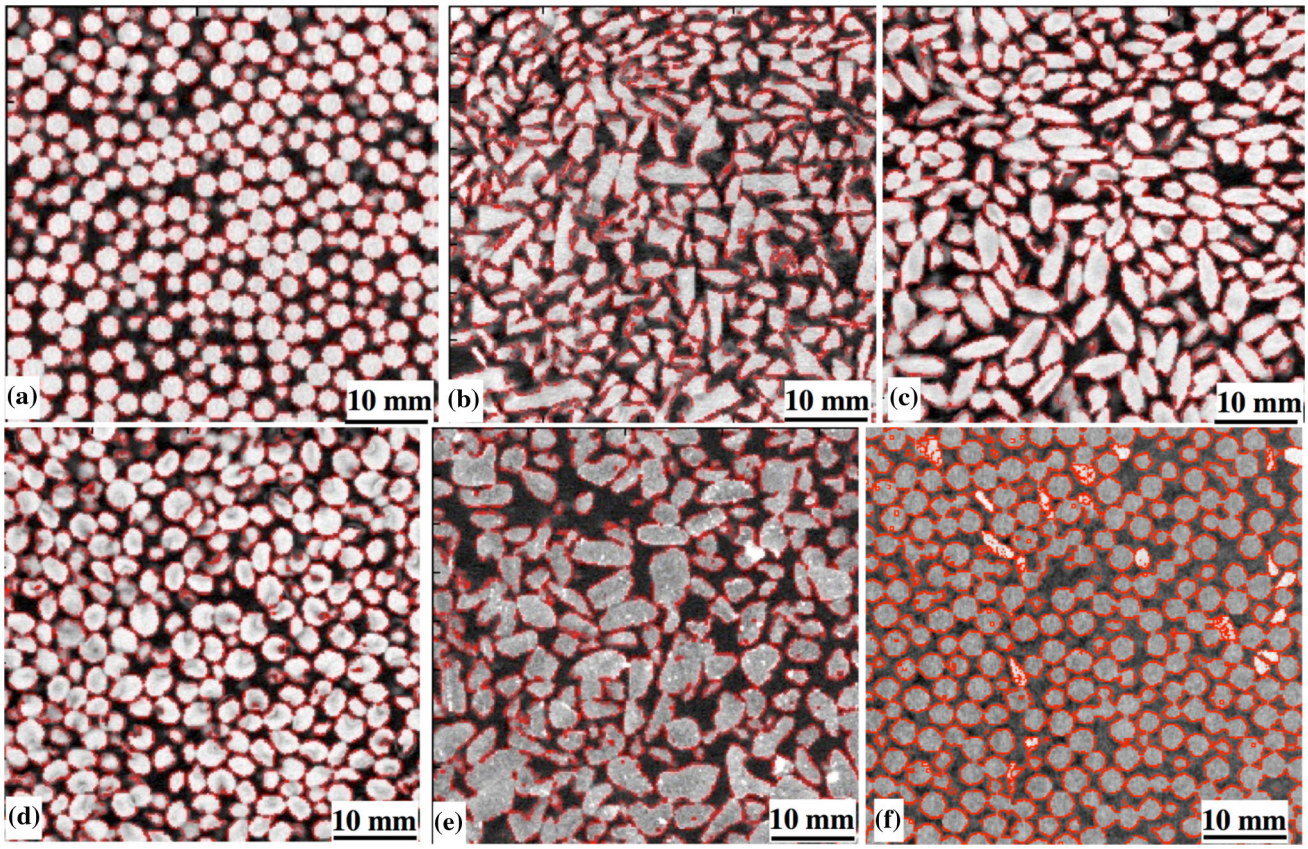

Fig. 5 Reconstructed cross-sections of the 5 tested granular materials **a** glass bead, **b** glass grit, **c** white rice, **d** sorghum, **e** Seramis and **f** mixture of glass bead and glass grit (4% in mass) (color figure online)

this particle shape analysis is the estimation of the goodness of the particles of the examined materials to be modelled by ellipsoidal shape (referred hereafter as the ellipsoidal shape goodness, γ). This is evaluated using the following expression:

$$\gamma = \frac{6V_p}{\pi V_c}, \tag{3}$$

where V_p is the volume of the particle and V_c is its so-called coffin box. We understand the notion of the coffin box as the tightest parallelepiped box that surrounds the particle. In eq. (3), a perfect ellipsoid particle will have $\gamma = 1$ since $V_c = 6V_p/\pi$. The coffin box is obtained by calculating the matrix of inertia of a particle and getting its eigenvectors that correspond to its principal axes. Along each principal direction the voxel boundaries are searched, which have the largest negative and positive vector rejections $[\mathbf{m_i}; \mathbf{M_i}]_{i=\{x,y,z\}}$ with respect to the particle centroid C_p, as schematized in Fig. 8a. Exemplar results for the five different tested granular materials are shown in Fig. 8b, where a good alignment of the coffin boxes along the main axis of the corresponding particles can be observed. The example of the coffin box of the glass bead is obviously not a matter of discussion, because of the isotropic nature of the particle.

The ellipsoidal shape goodness distribution for the five different tested granular materials is depicted in Fig. 9a. It is perfectly noticeable that the three materials which present the largest ellipsoidal shape goodness values are glass grit ($\langle\gamma\rangle = 0.9$), sorghum ($\langle\gamma\rangle = 0.86$) and white rice ($\langle\gamma\rangle = 0.81$), while the lowest goodness value was obtained for glass grit ($\langle\gamma\rangle = 0.6$). Valuable, complementary parameters allowing for the comparison of different granular materials are size and aspect ratio. Regarding the size, the smallest dimension of the coffin box, being its thickness, is considered, since it is the one that needs to be compared with voxel size for the sake of image quantification. The histogram shown in Fig. 9b indicates that sorghum presents the average size, which is the closest to monodispersed glass bead. Besides, its size scatter is small and it does not exceed 0.3 mm. Rice and glass grit have the particularity to present the smallest average thickness (35–50% smaller than glass bead diameter), having very large aspect ratio. Figure 9 shows a bivariate histogram of aspect ratio $F_{ab} = b/a$ and $F_{ac} = c/a$, where a, b and c are the thickness, width and length of particle coffin box, respectively. A strong anisotropy of rice grain shape can be

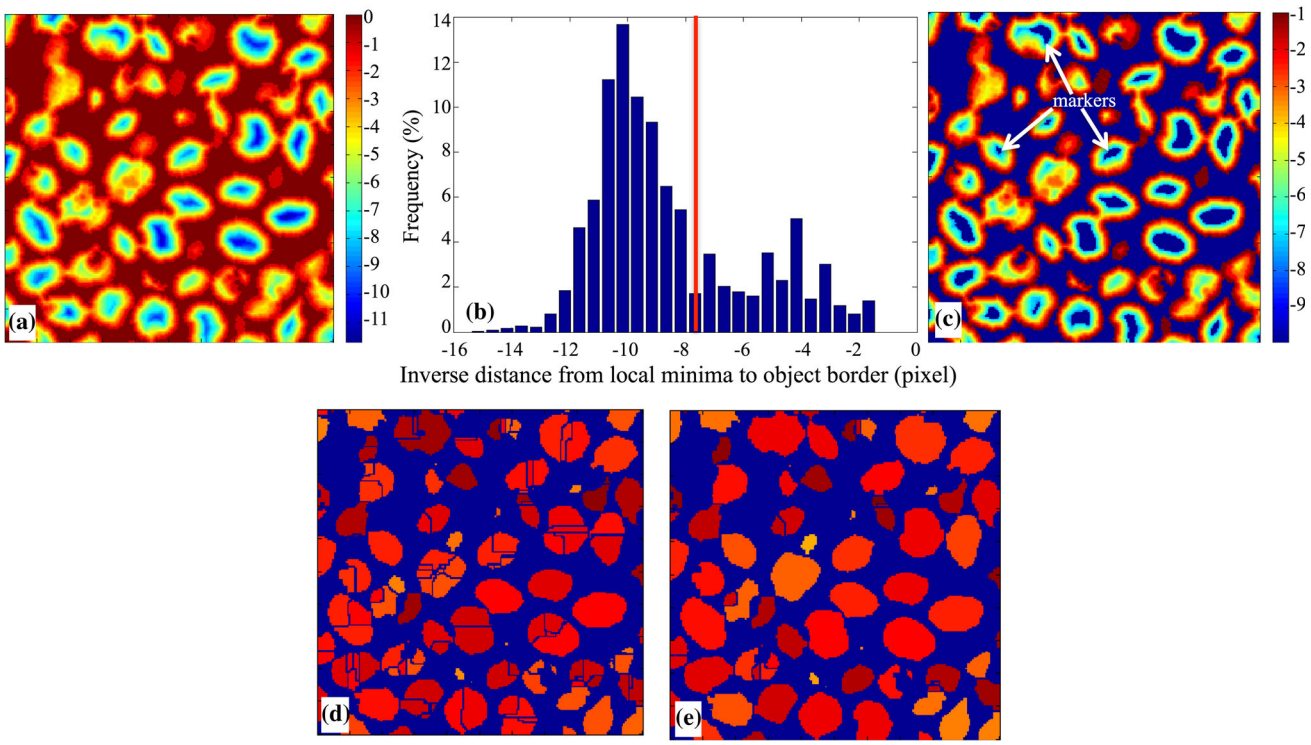

Fig. 6 Illustration of marker generation for watershed method—case of sorghum. **a** Inverse distance map, **b** histogram of inverse distance from local minima to object border—the red line indicates the threshold distance, **c** modified inverse distance map with island markers (dark blue), **d** segmentation result with standard watershed and **e** segmentation result with island marker-based watershed (color figure online)

observed in Fig. 9c, where $\langle F_{ac} \rangle \approx 2\langle F_{ab} \rangle = 3.1$ with a relatively narrow scatter for F_{ab} ($\Delta F_{ab} = 0.14$). The values are more scattered for glass grit, with the presence of three different shape populations, indicated by the red arrows on the histogram projection of F_{ac} superimposed in Fig. 9b. The selected elongated glass grit particle, shown in Fig. 8b, is a part of the smallest third population. Interestingly, we can see that glass bead and sorghum present the least scattered shape, with the latter presenting an oblate spheroid shape (i.e. $\langle F_{ac} \rangle \approx \langle F_{ab} \rangle = 1.6$) (Fig. 10).

3.4 Discussion: granular material selection

The topic of selection of granular material may look controversial from the point of view of material handling and conveying, since it is rather the container or silo design that is usually determined based on the given material properties and selected flow type. Jenike charts or DEM simulations are usually the principal tools applied for determination of mechanical characteristics of granular materials. However, when the numerical technic is considered, simulations are based not only on experimental data when they can be calculated (for instance macroscopic/microscopic friction properties $\mu_{s,w}$, $\Phi_{b,i}$, $\Phi_{b,w}$), but also mechanical contact model that includes different forces reflecting sliding friction or rolling friction. Recent models have considered the cases where particle rotation is allowed or not allowed to reflect the cases of spherical or non-spherical particle, the latter having the tendency to only rely on sliding to relieve stress under shear [47]. In other words, the lack of particle rotation would approximate more closely the movement of non-spherical particles, which have less rotational freedom due to mechanical interlocking. Knowing the particle-wall or particle–particle friction coefficients, one can estimate the macroscopic wall or internal friction angle, assuming that particles will or will not undergo rotation during gravitational movement. This is illustrated in Fig. 11 which shows how "no rotation" and "with rotation" relations can be used to predict wall friction angle $\Phi_{b,w}$ when particle-wall friction coefficient $\mu_{s,w}$ and particle shape are known. However, one can also confront this relationship graph with experimental measurements, as the ones presented in Sect. 3.2. While the results for glass bead, sorghum (oblate shape, nearly-spherical) or glass grit and Seramis (angular shape grains) are in agreement with the predictions, white rice, despite its anisotropic shape, perfectly lies on the "with rotation" curve. Therefore, the predicted ability of sorghum and white rice to roll during gravitational flow becomes an interesting topic to be investigated using quantitative X-ray tomography due to their non-spherical shape. Moreover, not only their X-ray

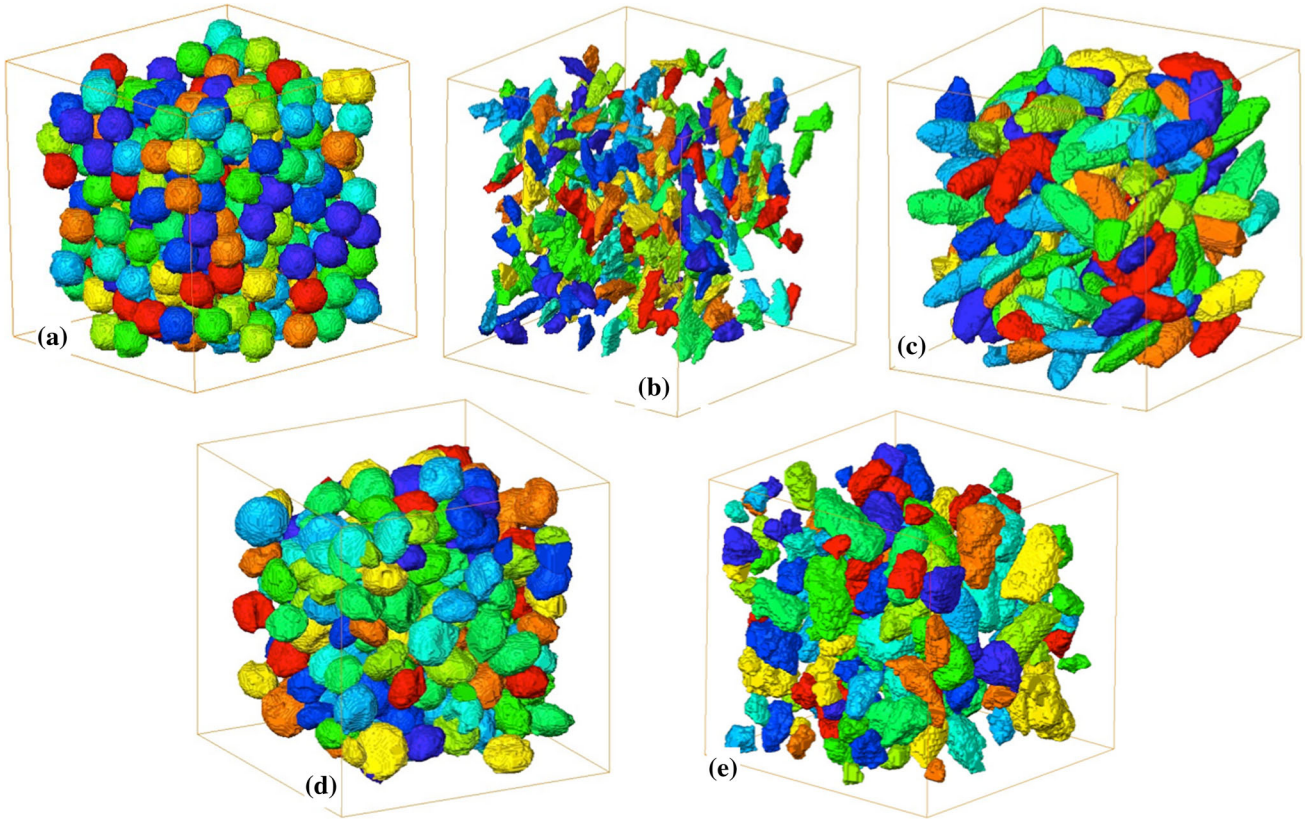

Fig. 7 3D rendering of the segmented grains after watershed-based processing method. All volumes are of size 200 × 200 × 200 voxels and objects categorised in 10 different labels for visualization ease. **a** Glass bead, **b** glass grit, **c** white rice, **d** sorghum and **e** Seramis (color figure online)

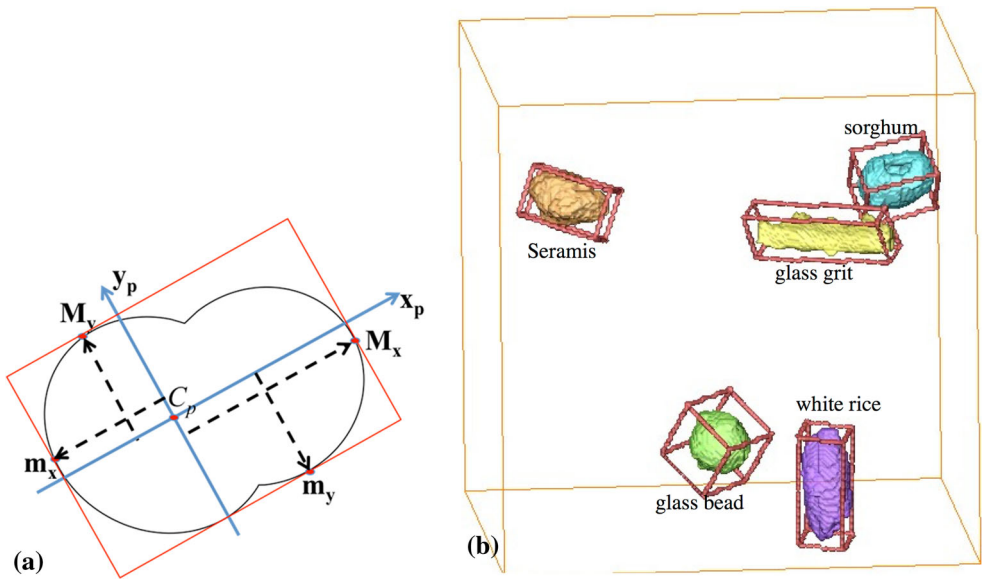

Fig. 8 Coffin box of particles. **a** 2D illustration how coffin box (in red) is obtained using vector rejections, **b** 3D rendering of 5 exemplar grains representing the tested granular materials and their respective coffin boxes (color figure online)

tomography images present very good contrast for boundary detection, but these two materials, as analysed in Sect. 3.3.2, also present high γ values, which make them adapted for DEM modelling with ellipsoids, even if the control of the contact model and its computation during silo discharging is

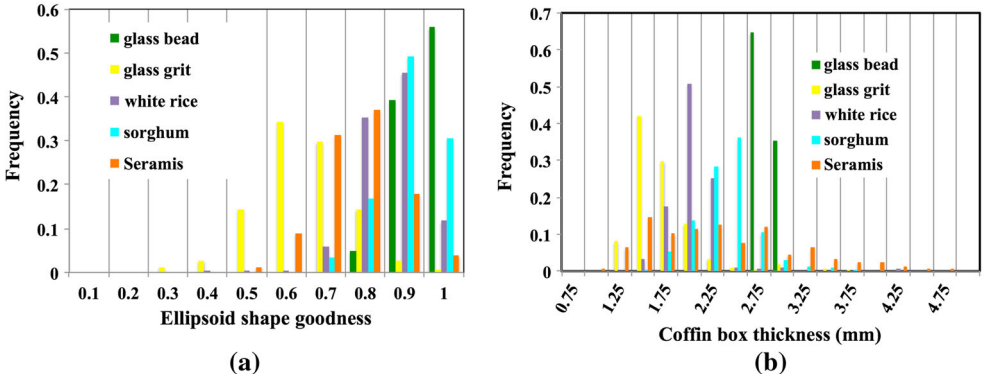

Fig. 9 Grain shape analysis for the five tested granular material. **a** Histogram of the ellipsoid shape goodness γ and **b** histogram of the coffin box thickness (color figure online)

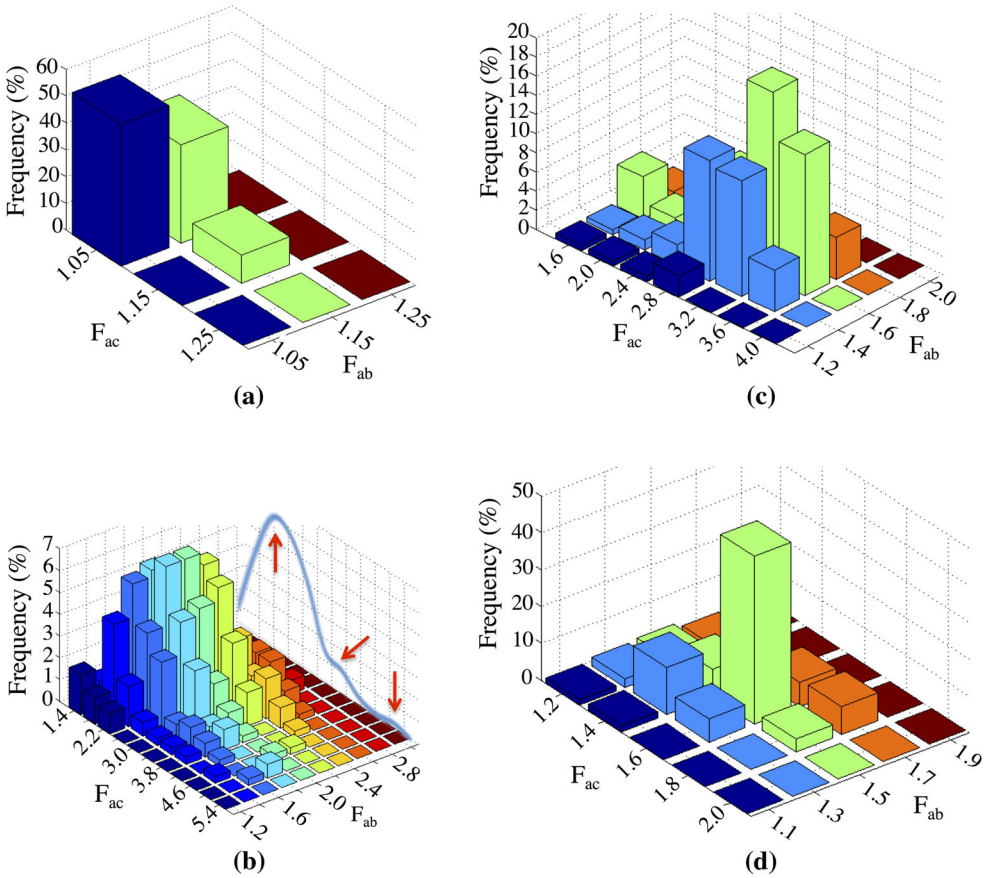

Fig. 10 Bivariate histogram of aspect ratio parameters F_{ab} and F_{ac} for the tested granular materials. **a** Glass bead, **b** glass grit, **c** white rice and **d** sorghum. In the case of (**b**), the histogram projection for F_{ac} is also displayed (color figure online)

more complex and more time consuming than for spherical bead [56].

This multi-parameter approach also suggests that, because of its low Young modulus E_s (fragile, tendency to erode during friction), large cohesion c (cohesive material due to rough surface) and lowest average ellipsoidal shape goodness γ (irregular shape that is difficult to model), Seramis is the granular material that is the least adapted to the future comparison between time-lapse X-ray tomography data and results of DEM analysis during silo discharging process of cohensionless material. The cohesiveness of the material during gravitational flow in silo has been recently observed, among other things, using the ultra-fast X-ray tomography system ROFEX [57]. The spherical shape of glass bead is also a drawback to investigate their rolling properties during flow. However, the fact that glass grit and glass bead present

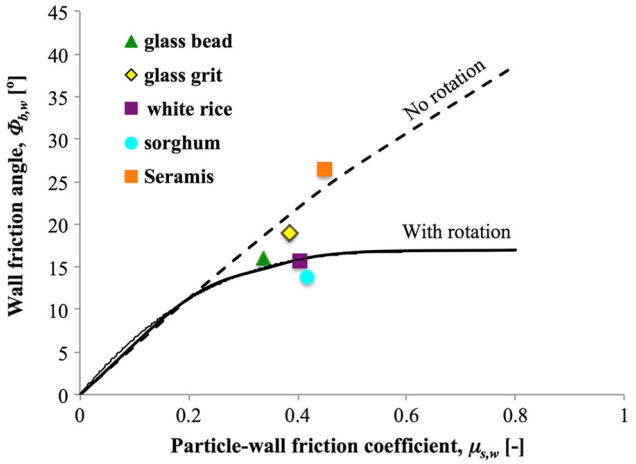

Fig. 11 Comparison of experimental wall friction angle and particle-wall coefficients of the five tested granular materials with DEM prediction of particle-wall interaction considering both freely rotating and non-rotating spheres [47] (color figure online)

a different attenuation in X-ray images makes the former a potential candidate for tracking purposes. Indeed, by injecting a small amount of glass grit with low aspect ratio, one can anticipate that the movements of these tracer particles will be representative of the surrounding media, i.e. glass bead. This is obviously a hypothesis that remains to be verified in future.

4 Conclusion

The following conclusions can be drawn from the present study:

- Granular materials of different origin: glass bead, glass grit, clay granules and short grain white rice, and sorghum, have been examined taking into account physical property measurements and X-ray tomographic imaging.
- The granular materials of biological origin, i.e. short grain white rice and sorghum, presented similar material and mechanical properties, e.g. density, compressibility, friction properties and elastic properties, which compete with properties of classical glass materials. The macroscopic and microscopic frictional properties of plant materials were found to fit well with DEM prediction of gravitational flow including rolling friction component.
- All tested materials are good candidates for X-ray tomography investigations, based on their relative low density and large grain size, which are adapted for most of the laboratory set-ups available on the market. However, the materials of biological origin are the ones which present the best contrast ratio. This is an important parameter to consider for image segmentation strategies, such as the watershed method, which aims at separating each grain for quantitative analysis.
- The quantitative shape analysis, which has mainly been based on the matrix of inertia of the extracted particles, has focused on studying particle aspect ratios and ellipsoidal shape modelling. This quantification has confirmed that, besides glass bead, rice and sorghum can also be satisfyingly modelled by ellipsoid.
- All the above-mentioned consideration put rice and sorghum as good research material for DEM simulations and time-lapse X-ray tomography imaging during gravitational flow studies such as silo discharge.

Acknowledgements This work is supported by the National Science Centre, Poland (NCN OPUS10 *2015/19/B/ST8/02773*).

Compliance with ethical standards

Conflict of interest The authors declare that they have no conflict of interest.

References

1. Steingart, D.A., Evans, J.W.: Measurements of granular flows in two-dimensional hoppers by particle image velocimetry. Part I: experimental method and results. Chem. Eng. Sci. **60**, 1043–1051 (2005). https://doi.org/10.1016/j.ces.2004.09.066
2. Gentzler, M., Tardos, G.I.: Measurement of velocity and density profiles in discharging conical hoppers by NMR imaging. Chem. Eng. Sci. **64**, 4463–4469 (2009). https://doi.org/10.1016/j.ces.2009.08.010
3. Babout, L., Grudzien, K., Maire, E., Withers, P.J.: Influence of wall roughness and packing density on stagnant zone formation during funnel flow discharge from a silo: an X-ray imaging study. Chem. Eng. Sci. **97**, 210–224 (2013). https://doi.org/10.1016/j.ces.2013.04.026
4. Grudzien, K., Niedostatkiewicz, M., Adrien, J., Maire, E., Babout, L.: Analysis of the bulk solid flow during gravitational silo emptying using X-ray and ECT tomography. Powder Technol. **224**, 196–208 (2012). https://doi.org/10.1016/j.powtec.2012.02.054
5. Artoni, R., Zugliano, A., Primavera, A., Canu, P., Santomaso, A.: Simulation of dense granular flows: comparison with experiments. Chem. Eng. Sci. **66**, 548–557 (2011). https://doi.org/10.1016/j.ces.2010.11.029
6. Anand, A., Curtis, J.S., Wassgren, C.R., Hancock, B.C., Ketterhagen, W.R.: Predicting discharge dynamics from a rectangular hopper using the discrete element method (DEM). Chem. Eng. Sci. **63**, 5821–5830 (2008). https://doi.org/10.1016/j.ces.2008.08.015
7. Nikitidis, M.S., Tuzun, U., Spyrou, N.M.: Measurement of size segregation by self-diffusion in slow-shearing binary mix-

ture flows using dual photon gamma-ray tomography. Chem. Eng. Sci. **53**, 2335–2351 (1998). https://doi.org/10.1016/s0009-2509(98)00070-0
8. Wiącek, J., Molenda, M., Ooi, J.Y., Favier, J.: Experimental and numerical determination of representative elementary volume for granular plant materials. Granul. Matter **14**, 449–456 (2012). https://doi.org/10.1007/s10035-012-0351-2
9. Wiącek, J., Molenda, M.: Moisture-dependent physical properties of rapeseed—experimental and DEM modeling. Int. Agrophys. **25**, 59–65 (2011)
10. Sielamowicz, I., Balevičius, R.: Experimental and computational analysis of granular material flow in model silos., Warsaw (2013)
11. Horabik, J., Molenda, M.: Parameters and contact models for DEM simulations of agricultural granular materials: a review. Biosyst. Eng. **147**, 206–225 (2016). https://doi.org/10.1016/j.biosystemseng.2016.02.017
12. al Mahbub, A., Haque, A.: X-ray computed tomography imaging of the microstructure of sand particles subjected to high pressure one-dimensional compression. Materials (Basel) **9**, 890 (2016). https://doi.org/10.3390/ma9110890
13. McDonald, S.A., Schneider, L.C.R., Cocks, A.C.F., Withers, P.J.: Particle movement during the deep penetration of a granular material studied by X-ray microtomography. Scr. Mater. **54**, 191–196 (2006). https://doi.org/10.1016/j.scriptamat.2005.09.042
14. McDonald, S.A., Harris, D., Withers, P.J.: In-situ X-ray microtomography study of the movement of a granular material within a die. Int. J. Mater. Res. (formerly Zeitschrift fuer Met.) **103**, 162–169 (2012). https://doi.org/10.3139/146.110672
15. Alikarami, R., Andò, E., Gkiousas-Kapnisis, M., Torabi, A., Viggiani, G.: Strain localisation and grain breakage in sand under shearing at high mean stress: insights from in situ X-ray tomography. Acta Geotech. **10**, 15–30 (2015). https://doi.org/10.1007/s11440-014-0364-6
16. Desrues, J., Andò, E.: Strain localisation in granular media. Comptes Rendus Phys. **16**, 26–36 (2015). https://doi.org/10.1016/j.crhy.2015.01.001
17. Alshibli, K.A., Sture, S., Frank, M.L., Lankton, M.R., Batiste, S.N., Swanson, R.A., Costes, N.C.: Assessment of localized deformations in sand using X-ray computed tomography. Geotech. Test. J. **23**, 274–299 (2000)
18. Wegner, S., Stannarius, R., Boese, A., Rose, G., Szabó, B., Somfai, E., Börzsönyi, T.: Effects of grain shape on packing and dilatancy of sheared granular materials. Soft Matter **10**, 5157 (2014). https://doi.org/10.1039/c4sm00838c
19. Hasan, A., Alshibli, K.A.: Experimental assessment of 3D particle-to-particle interaction within sheared sand using synchrotron microtomography. Géotechnique **60**, 369–379 (2010). https://doi.org/10.1680/geot.2010.60.5.369
20. Mueth, D.M., Debregeas, G.F., Karczmar, G.S., Eng, P.J., Nagel, S.R., Jaeger, H.M.: Signatures of granular microstructure in dense shear flows. Nature **406**, 385–389 (2000). https://doi.org/10.1038/35019032
21. Börzsönyi, T., Somfai, E., Szabó, B., Wegner, S., Mier, P., Rose, G., Stannarius, R.: Packing, alignment and flow of shape-anisotropic grains in a 3D silo experiment. New J. Phys. **18**, 93017 (2016). https://doi.org/10.1088/1367-2630/18/9/093017
22. Luding, S., Manetsberger, K., Müllers, J.: A discrete model for long time sintering. J. Mech. Phys. Solids. **53**, 455–491 (2005). https://doi.org/10.1016/j.jmps.2004.07.001
23. Bharadwaj, R.: Using DEM to solve bulk material handling problems. Chem. Eng. Prog. **108**, 54–58 (2012)
24. Wang, Y., Alonso-Marroquin, F., Guo, W.W.: Rolling and sliding in 3-D discrete element models. Particuology **23**, 49–55 (2015). https://doi.org/10.1016/j.partic.2015.01.006
25. Skinner, A.E.: A note on the influence of interparticle friction on the shearing strength of a random assembly of spherical particles. Géotechnique **19**, 150–157 (1969). https://doi.org/10.1680/geot.1969.19.1.150
26. Mair, K., Frye, K.M., Marone, C.: Influence of grain characteristics on the friction of granular shear zones. J. Geophys. Res. Solid Earth **107**, ECV 4-1–ECV 4-9 (2002). https://doi.org/10.1029/2001JB000516
27. Härtl, J., Ooi, J.Y.: Experiments and simulations of direct shear tests: porosity, contact friction and bulk friction. Granul. Matter **10**, 263–271 (2008). https://doi.org/10.1007/s10035-008-0085-3
28. Härtl, J., Ooi, J.Y.: Numerical investigation of particle shape and particle friction on limiting bulk friction in direct shear tests and comparison with experiments. Powder Technol. **212**, 231–239 (2011). https://doi.org/10.1016/j.powtec.2011.05.022
29. Cao, Y.X., Chakrabortty, B., Barker, G.C., Mehta, A., Wang, Y.J.: Bridges in three-dimensional granular packings: experiments and simulations. EPL Europhys. Lett. **102**, 24004 (2013). https://doi.org/10.1209/0295-5075/102/24004
30. Tai, C.H., Hsiau, S.S., Kruelle, C.A.: Density segregation in a vertically vibrated granular bed. Powder Technol. **204**, 255–262 (2010). https://doi.org/10.1016/j.powtec.2010.08.010
31. González-Montellano, C., Ramírez, Á., Gallego, E., Ayuga, F.: Validation and experimental calibration of 3D discrete element models for the simulation of the discharge flow in silos. Chem. Eng. Sci. **66**, 5116–5126 (2011). https://doi.org/10.1016/j.ces.2011.07.009
32. Hutter, K., Koch, T., Pluuss, C., Savage, S.B.: The dynamics of avalanches of granular materials from initiation to runout. Part II. Experiments. Acta Mech. **109**, 127–165 (1995). https://doi.org/10.1007/BF01176820
33. Li, Y., Xu, Y., Jiang, S.: DEM simulations and experiments of pebble flow with monosized spheres. Powder Technol. **193**, 312–318 (2009). https://doi.org/10.1016/j.powtec.2009.03.009
34. Li, Y., Xu, Y., Thornton, C.: A comparison of discrete element simulations and experiments for "sandpiles" composed of spherical particles. Powder Technol. **160**, 219–228 (2005). https://doi.org/10.1016/j.powtec.2005.09.002
35. Kobylka, R., Molenda, M.: DEM modelling of silo load asymmetry due to eccentric filling and discharge. Powder Technol. **233**, 65–71 (2013). https://doi.org/10.1016/j.powtec.2012.08.039
36. Parafiniuk, P., Molenda, M., Horabik, J.: Discharge of rapeseeds from a model silo: physical testing and discrete element method simulations. Comput. Electron. Agric. **97**, 40–46 (2013). https://doi.org/10.1016/j.compag.2013.06.008
37. Gallego, E., Ruiz, A., Aguado, P.J.: Simulation of silo filling and discharge using ANSYS and comparison with experimental data. Comput. Electron. Agric. **118**, 281–289 (2015). https://doi.org/10.1016/j.compag.2015.09.014
38. Sielamowicz, I., Czech, M., Kowalewski, T.A.: Empirical description of flow parameters in eccentric flow inside a silo model. Powder Technol. **198**, 381–394 (2010). https://doi.org/10.1016/j.powtec.2009.12.003
39. Sielamowicz, I., Czech, M., Kowalewski, T.A.: Empirical description of granular flow inside a model silo with vertical walls. Biosyst. Eng. **108**, 334–344 (2011). https://doi.org/10.1016/j.biosystemseng.2011.01.004
40. Anon: Compression test of food materials of convex shape. ASAE S368.4 DEC (2000). In: ASAE Standards. The American Society of Agricultural Engineers, St Joseph (2001)
41. Basis of design and actions on structures. Part 4. Actions in silos and tanks. In: Eurocode 1 (2006)
42. Kak, A.C., Slaney, M.: Principles of Computerized Tomographic Imaging. IEEE Press, New York (1987)
43. Feldkamp, L.A., Davis, L.C., Kress, J.W.: Practical cone-beam algorithm. J. Opt. Soc. Am. A **1**, 612–619 (1984)
44. Wellington, S.L., Vinegar, H.J.: X-ray computerized tomography. J. Pet. Technol. **39**, 885–898 (1987). https://doi.org/10.2118/16983-PA

45. Babout, L.: Link to X-ray tomography data (radiographs, reconstructed volumes) of granular materials (glass bead, glass grit, sorghum, short-grain rice and Seramis), http://lbabout.iis.p.lodz.pl/Research_interests_and_projects_files/files/granular_flow_Tomo_DEM/Tomo_Gdansk/GM_tomo.tar
46. Cho, G.-C., Dodds, J., Santamarina, J.C.: Particle shape effects on packing density, stiffness, and strength: natural and crushed sands. J. Geotech. Geoenviron. Eng. **132**, 591–602 (2006). https://doi.org/10.1061/(ASCE)1090-0241(2006)132:5(591)
47. Ketterhagen, W.R., Curtis, J.S., Wassgren, C.R., Hancock, B.C.: Predicting the flow mode from hoppers using the discrete element method. Powder Technol. **195**, 1–10 (2009). https://doi.org/10.1016/j.powtec.2009.05.002
48. Cleary, P.W.: The effect of particle shape on simple shear flows. Powder Technol. **179**, 144–163 (2008). https://doi.org/10.1016/j.powtec.2007.06.018
49. Poschel, T., Buchholtz, V.: Static friction phenomena in granular materials: Coulomb law versus particle geometry. Phys. Rev. Lett. **71**, 3963–3966 (1993). https://doi.org/10.1103/PhysRevLett.71.3963
50. Fu, X., Elliott, J.A., Bentham, A.C., Hancock, B.C., Cameron, R.E.: Application of X-ray microtomography and image processing to the investigation of a compacted granular system. Part. Part. Syst. Charact. **23**, 229–236 (2006). https://doi.org/10.1002/ppsc.200601054
51. Vlahinić, I., Andò, E., Viggiani, G., Andrade, J.E.: Towards a more accurate characterization of granular media: extracting quantitative descriptors from tomographic images. Granul. Matter **16**, 9–21 (2014). https://doi.org/10.1007/s10035-013-0460-6
52. Marmottant, A., Salvo, L., Martin, C.L., Mortensen, A.: Coordination measurements in compacted NaCl irregular powders using X-ray microtomography. J. Eur. Ceram. Soc. **28**, 2441–2449 (2008). https://doi.org/10.1016/j.jeurceramsoc.2008.03.041
53. Gillman, A., Matouš, K., Atkinson, S.: Microstructure-statistics-property relations of anisotropic polydisperse particulate composites using tomography. Phys. Rev. E. **87**, 22208 (2013). https://doi.org/10.1103/PhysRevE.87.022208
54. Faessel, M., Jeulin, D.: Segmentation of 3D microtomographic images of granular materials with the stochastic watershed. J. Microsc. **239**, 17–31 (2010). https://doi.org/10.1111/j.1365-2818.2009.03349.x
55. Soille, P.: Morphological Image Analysis. Springer, Berlin (2003)
56. Houlsby, G.T.: Potential particles: a method for modelling non-circular particles in DEM. Comput. Geotech. **36**, 953–959 (2009). https://doi.org/10.1016/j.compgeo.2009.03.001
57. Waktola, S., Bieberle, A., Barthel, F., Bieberle, M., Hampel, U., Grudzień, K., Babout, L.: A new data-processing approach to study particle motion using ultrafast X-ray tomography scanner: case study of gravitational mass flow. Exp. Fluids **59**, 69 (2018). https://doi.org/10.1007/s00348-018-2523-2